

Spectroscopic and Magnetic performance of Cobalt (Co) Incorporated $\text{NiMn}_{0.05}\text{Fe}_{1.95}\text{O}_4$ Nanoferrites: A potent antifungal activity against *Aspergillus niger* (MT675916).

Sapna Thakur

Eternal University

Geetika Guleria

Eternal University

Shweta Thakur

Lingayas University: Lingayas Vidyapeeth

Sushma Sharma

Eternal University

Poonam Kumari (✉ p19phy@gmail.com)

Eternal University <https://orcid.org/0000-0001-6171-3790>

Research Article

Keywords: Spinel ferrite NPs, Structural properties, Magnetic properties, Antifungal activity

Posted Date: April 21st, 2021

DOI: <https://doi.org/10.21203/rs.3.rs-405237/v1>

License:  This work is licensed under a Creative Commons Attribution 4.0 International License. [Read Full License](#)

Abstract

We investigated the impact of cobalt (Co) incorporation on the structural, optical, and magnetic properties of ferrite $\text{Ni}_{1-x}\text{Co}_x\text{Mn}_{0.05}\text{Fe}_{1.95}\text{O}_4$, also known as NCMF for $x = 0, 0.02, \text{ and } 0.04$, which were successfully synthesized using a low-temperature sol gel combustion process with nitrates as cations and citric acid ($\text{C}_6\text{H}_8\text{O}_7$) as the combustion/chelating agent. In X-ray diffraction studies, cobalt incorporation resulted in a significant increase in lattice parameter from 8.31 to 8.36, as well as a significant increase in density from 5.42 to 5.52 g/cm^3 ; crystal size formation was observed in the range of 44.76 nm to 48.54 nm for all samples. Raman spectra analysis confirmed that single phase belongs to the $\text{Fd}3\text{m}$ space group. Fourier transform infrared (FTIR) spectra were used to identify functional clusters and residual groups in all samples. UV-visible spectroscopy showed a redshift of 0.92 eV for $x = 0.04$. The effect of dopants on nickel ferrites' magnetization was observed in the range 52emu/g – 59emu/g, indicating that all samples contain soft magnetic content. Antifungal activity of synthesized sample was analyzed against *Aspergillus niger* (MT675916) species of plant pathogenic fungi isolated from Capsicum during storage. Biological analysis designated that the sample for $x = 0.04$ has shown a 100% potent antifungal activity against *Aspergillus niger* (MT675916) species. For $x = 0.04$ treatment completely inhibit the growth of fungus after 7 days. Therefore, NCMF NPs can be used as applicant resources for industrial, medical, and biological applications.

Introduction

Ferrites are large magnetic nanoparticles (NPs) with a spinel structure. Magnetic hyperthermia, magnetically driven drug delivery, magnetic resonance imaging, and antimicrobials are just some of the biomedical applications for spinel ferrite NPs (Pu et al. 2016, Prathapani et al. 2014, Mukherjee et al. 2013). By varying their size and chemical composition, ferromagnetic spinel ferrites nanoparticles with the general chemical formula MFe_2O_4 (where $\text{M} = \text{Co}^{2+}, \text{Ni}^{2+}, \text{Mn}^{2+}, \text{Zn}^{2+}$, etc.) give great magnetic property tunability. Besides, Spinel ferrite is chemically represented as $\text{M}^{2+}\text{Fe}^{3+}\text{O}_4$ (Orozco et al. 2017), where M and Fe are divalent and trivalent cations; the properties of the ferrites can be tuned by changing the ions at tetrahedral (A site) and octahedral (B site). As an earlier investigation, Manganese (Mn) (Kadam et al. 2013; Shobana & Sankar 2009; Sharma et al. 2021) doped nickel ferrite having formula $\text{Ni}_{1-x}\text{Mn}_x\text{Fe}_2\text{O}_4$ for $x = 0.05, 0.10, 0.15$ were prepared through chemical co-precipitation. Furthermore, low magneto-cryatalline anisotropy along with ferrimagnetic behavior make NMFO a potential candidate material for “candidate for biomedical industries” applications [6]. There have been fewer reports which deal with the effect of Co ions doping on the various properties of the $\text{Ni}_{0.95}\text{Mn}_{0.05}\text{Fe}_2\text{O}_4$ ferrites (Chand et al. 2017). In this context, efforts in this work have directed to synthesize Co concentration effect on spinel ferrites with the chemical formula $\text{Ni}_{1-x}\text{Co}_x\text{Mn}_{0.05}\text{Fe}_{1.95}\text{O}_4$ ($x = 0.0, 0.02, 0.04$) prepared by low temperature sol-gel combustion method. Furthermore, Due to the increasing microbial resistance to antibiotics and the improvement of resistant strains, magnetic nanoparticles are one of the most promising materials because of their exceptional antibacterial properties due to their wide surface area to volume ratio, which excites researchers about this because of the growing microbial resistance to antibiotics and the improvement of resistant strains; very high antibacterial properties to meet the requirements of a drug delivery system such that antibiotic concentrations are kept to a minimum. Recently numerous studies have been done to analyse the antimicrobial efficacy of differently synthesized nanomaterials (Khan et al. 2021). Zerovalent Cobalt and Nickel nanocomposites integrated with chitosan-humic acid were analysed for its antifungal efficacy against *C. albicans*, *C. glabrata*, *C. tropicalis* and *C. parapsilosis* species (Akinremi et al. 2018). Nickel polyaniline/cellulose bio-nanocomposites demonstrated significant degradation of reactive orange (RO-16) dye under visible light and the materials was found effective against two pathogenic fungi *Rhizoctonia solani* and *Alternaria alternate* (Ahmad et al. 2019). Several methods have been used to synthesise NPs nickel ferrites, but this is the first paper that we are aware of that reports the synthesis of Co ions doping on Ni, MnFe_2O_4 NPs using a sol gel process with nitrates precursors. This article presents an easy, low cost and environmentally friendly synthesis method to obtain NPs of ferrite and the study of their antifungal effect against *Aspergillus niger* isolated from Capsicum during storage. A better understanding of the structure, optical, magnetic properties and antifungal activity of samples is, therefore, highly beneficial to tune the properties for desired electronic and biomedical applications.

Materials And Methods

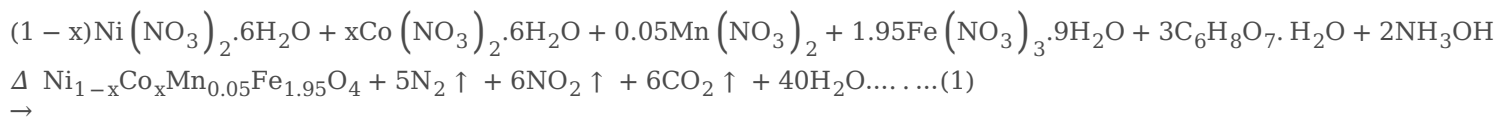
Chemicals used

Nickel nitrate [$\text{Ni}(\text{NO}_3)_2 \cdot 6\text{H}_2\text{O}$], Cobalt nitrate [$\text{Co}(\text{NO}_3)_2 \cdot 2\text{H}_2\text{O}$], Manganese nitrate [$\text{Mn}(\text{NO}_3)_2$], Iron (III) nitrate [$\text{Fe}(\text{NO}_3)_3 \cdot 9\text{H}_2\text{O}$] were used as starting materials for the synthesis of NCMF materials, and Citric acid [$\text{C}_6\text{H}_8\text{O}_7 \cdot \text{H}_2\text{O}$] was used as a combustion agent. Ammonium

hydroxide [NH₃OH] was used to regulate the pH; and the study of their antifungal effect in vitro against two pathogenic fungi *Rhizoctonia solani* and *Alternaria alternata*, isolated from the stored capsicum on the sterilized potato dextrose agar (PDA) medium.

Synthesis of Ferrite NPs.

NPs of Ni_{1-x}Co_xMn_{0.05}Fe_{1.95}O₄ [NMFO] with x = 0, 0.02, 0.04, were synthesized by sol-gel autocombustion method. Analytical reagent (AR) grade Ni(NO₃)₂·6H₂O, Fe(NO₃)₃·9H₂O, Co(NO₃)₃·6H₂O, and citric acid (C₆H₈O₇·H₂O) were used as raw precursors. Stoichiometric amounts of metal nitrates and citric acid with 1:1 ratio were dissolved in deionized water to form the citrate-nitrate solution. Drop by drop, ammonium hydroxide was added to neutralise the solution. To homogenise the solution and form the citric acid and metal nitrates mixture for the combustion reaction, it was stirred on a magnetic stirrer at 40°C. Then obtained solution was dried out slowly on a hot plate stirrer at a temperature 80°C with continuous stirring until the viscous gel was formed. On further heating, the temperature of the gel increased to 200°C and autoignition of gel took place with the evolution of gases and a black powder was founded. The fine powder of samples was finally pre-sintered at 600°C for 3 h. Thus the weight of the powder obtained was reduced and the percentage yields were calculated from the total expected based on the solution concentration and the volume that was ~ 96% of total sample. For all NCMF samples, **Fig. 1** depicted a graphical depiction of the sol gel combustion preparation technique. In accordance with the obtained results, the following balanced chemical reaction is proposed for ferrite formation.



Characterization of Ferrite NPs

Phase identification and structural analyses of the prepared NPs were carried out by X-ray diffractometer XRD: RIGAKU-D/MAX-2400) in the range 20°- 80o using Cu K α radiation and wavelength of $\lambda = 0.154056$ nm. The phase transitional characteristics and structural modulation of prepared samples were measured by Raman Spectroscopy. FTIR study was done at IIT, Mandi by Fourier Transform Infra-Red Spectrophotometer Model RZX (Perkin Elmer). To measure the optical band gaps by UV-Visible spectrum was recorded via UV-Vis spectrometer Shimadzu (Asia Pacific) Pte. Ltd and Model UV - 2450 at IIT Mandi. The magnetic properties measurement made on crystalline powder via vibratory sample magnetometer (VSM) at room temperature (RT).

Antifungal activity measurement

Isolation of fungi *Aspergillus niger*

The fungi *Aspergillus niger* was isolated from the stored capsicum on the sterilized potato dextrose agar (PDA) medium. Using a sterilized scalpel about 2–3 mm small bits were cut. 0.5 per cent hypochlorite solution was used for sterilization of the bits for 30 Sec. only and then washed thoroughly with sterile distilled water. Under aseptic conditions, sterilised bits were placed on PDA plates. The inoculated plates were incubated at 25 ± 2°C for obtaining fungal growth. The cultures were purified from the inoculated culture on PDA plates or in slants and were sub cultured regularly after 15 days' interval of time (Diba et al. 2007).

Microscopic and molecular characterization of *Aspergillus niger*

Microscopic examinations were studied after interval of 1–2 weeks of incubation. A loopful normal saline was placed on a clean glass slide and a portion of cottony growth was transferred aseptically. The wet mounts were observed in compound bright field light microscope. The morphological characteristics i.e. hyphae structure, spores, arrangement of spores, etc. were recorded. In molecular characterization a region of the nuclear rDNA gene containing the ITS regions was amplified from the genomic DNA by PCR using the primer combinations ITS 4 (5'-TCC TCC GCT TTA TTG ATA TGC 3')/ ITS 6 (3'-GAA GGT GAA GTC GTA ACA AGG 5') (Zhao et al. 2004; Guillemaut & Maréchal-Drouard 1992). The ITS regions were amplified by ITS4/ITS6 primers ranged from 565 ~ 615 bp in the isolate. On BLAST, isolates showed high homologies (96 ~ 100%) with *Aspergillus niger*. The sequences were submitted to NCBI and its GenBank Accession Number is *Aspergillus niger* (MT675916).

In vitro evaluation of different treatments against pathogen

The efficacy of $\text{Ni}_{1-x}\text{Co}_x\text{Mn}_{0.05}\text{Fe}_{1.95}\text{O}_4$, referred to NCMF for $x = 0, 0.02, 0.04$ were tested against the pathogen. The double strength PDA medium by adding double concentration of PDA medium in water and this medium was sterilized in autoclave for 20 minutes. Simultaneously, double concentrations of treatments were also prepared by adding sterilized distilled water. So, as to get the desired concentration, double strength PDA medium and treatment solution were mixed. After blotting dry with sterilized filtered paper these bits were transferred and inoculated in the petri plates. A separate control treatment was also maintained in which only sterilized distilled water was added to double strength medium. Each treatment was replicated thrice and incubated in BOD incubator at $27 \pm 1^\circ\text{C}$ temperature. When control plates were fully covered with mycelium of the pathogen then the colony diameter of test pathogen was recorded. The per cent inhibition in the mycelial growth of the pathogen was calculated according to the formula given by Vincent, 1947 (Vincent 1947). $I = \frac{C-T}{C} \times 100$ where, I- Inhibition of mycelial growth (%), C- Linear mycelial growth in control (mm) after 24 hrs, T- Linear mycelial growth in treatment (mm) after 24 hrs. The above experiment was carried out in Completely Randomized Design (CRD) and the data were recorded after every 24 hrs till the full growth of fungus was obtained in control treatment.

Results And Discussion

XRD of the as-synthesized of NCMF Ferrites

The XRD patterns of $\text{Ni}_{1-x}\text{Co}_x\text{Mn}_{0.05}\text{Fe}_{1.95}\text{O}_4$ ($x = 0, 0.02, 0.04$) are shown in Fig. 2. Indexing of the patterns was made using the JCPDS data: 10-325 (NiFe_2O_4). It is evident (Fig. 2) that the XRD data confirms the formation of a face centered cubic spinel structure with the space group $\text{Fd}3\text{m}$ (Deng et al. 2019). An interesting observation is the fact that the formation of a single-phase cubic spinel structure occurs, where no other diffraction peaks corresponding to the impurity or any other phase present. An increase in the lattice constant is first, and reduction in the crystallite size is later. The lattice constant increases from 8.31 \AA ($x = 0.0$) to 8.36 \AA with increasing Co content $x = 0$ to 0.04 . Furthermore, the intense (311) peak shows a lower angle with increasing Co content (Fig. 2a), similar results have been reported in the literature (Mostaghni & Abed 2017). The (311) peak shift coupled with a linear increase in the lattice constant is mainly due to the replacement of smaller Ni^{2+} (0.69 \AA) and Fe^{3+} (0.64 \AA) by the larger Co^{2+} (0.78 \AA) in NiFe_2O_4 spinel lattice.

Differences in the ionic radii of Ni^{2+} , Fe^{3+} , and Co^{2+} ions can result in lattice strain (Naughton & Clarke 2007) which accounts for measurement of the distribution of lattice constants arising from crystal imperfections such as lattice dislocations or sinter stresses, stacking faults, lattice parameter and hence, unit cell expansion. Such effect is mainly due to the larger Co^{2+} ion substitution for Fe^{3+} in nickel ferrite. According to Williamson-Hall (Aly et al. 2016) plot (Fig. 1b), the lattice strain (ϵ) of samples are 2.51×10^{-3} - 2.31×10^{-3} with increasing Co content. The density of the samples was also calculated from XRD data by using $a = [d^2(h^2 + k^2 + l^2)]^{1/2}$, $V = a^3$

$\rho_{\text{eff}} = \frac{nM}{Na^3}$; where M is the molecular weight, N is the Avogadro number, n is the no. of formula units per unit cell, m is the mass, r is the radius and h is the thickness of the pellet. The density variation of NCMF compounds with Co context (x) is shown in Fig. 1(c). It is evident that ρ_{Xrd} increases with increasing Co content (x). The two important general remarks that can be derived from density variation of NCMF compounds are as follows. Effective incorporation of Co into NMF and completeness of the sintering process to the best possible extent is the first. Later is the density increase with Co concentration. The density and atomic weight of Co^{2+} are 8.9 gram/cm^3 and 58.93 , which are greater than those of Fe^{3+} 7.874 g/cm^3 and 55.845 . Thus, the overall density increase of NCMF compounds can attributed to the fact that the density and atomic weight of Co are higher than those of Fe for which the Co ions are substituting/replacing in NFO. Rahman et. al. reported that density increase are due to density and atomic weight of dopant is larger than that of Fe (Rahman et al. 2014). Finally, to understand the effect of Co on the crystal growth and kinetics, the variation in average crystallite size of the NCMF samples was considered. The crystallite size (d) was calculated from the integral width of the diffraction lines using the Scherrer's equation after background subtraction and correction for instrumental broadening (Cullity & Stock 2001). The Scherrer equation is: $d = 0.9\lambda/\beta\cos\theta$; where d is the grain size, λ is the wavelength of X-rays, β is the width of a peak at half of its intensity, and θ is the angle of the peak. The variation of crystallite size with x(Mo) is presented in Fig. 1(c). The corresponding crystallite size decreases. It can be noted that the crystallite size is in the range of from 48.54 nm ($x = 0.0$) to 40.76 nm ($x = 0.04$) for NCMF. It is important to recognize that the Mo incorporation induces the crystallite size increase, which can be due to difference in the ionic radius of Co compared to Fe in NCMF. The lattice strain, lattice parameter, density and average size values determined from XRD are listed in **Table I**.

SEM of NCMF Ferrites

SEM images of $\text{Ni}_{1-x}\text{Co}_x\text{Mn}_{0.05}\text{Fe}_{1.95}\text{O}_4$ prepared by the sol-gel combustion method are shown in Fig. 3 (a-b). The particle morphology was similar in all samples, which were semi-spherical and aggregated, but the particle size was different. The interaction of magnetic NPs with high surface energies resulted in the appearance of some agglomerated regions in SEM images (Naseri et al. 2013). EDX was used to validate the elemental composition of $\text{Ni}_{1-x}\text{Co}_x\text{Mn}_{0.05}\text{Fe}_{1.95}\text{O}_4$ NPs (Fig. 4(a-c)). Fe, Ni, Co, Mn and O elements were present in the study, with weight percentages have been shown by insight table of Fig. 4(a-c).

Raman spectroscopy of NCMF Ferrites

The Raman spectra of all prepared samples with the space group (Fd3m) crystallises in spinel structure with eight formula units per unit cell are shown in Fig. 5. The complete cubic symmetry unit cell has 56 atoms, but the smallest Bravais cell has just 14 atoms. The tetrahedral A-site contains half of the Co^{3+} and Ni^{2+} cations, while the octahedral B-site contains the remaining Mn^{4+} and Fe^{3+} cations. It has five Raman active modes based on group theory (Velhal et al. 2015). It should be noted that Raman peaks in the $620\text{--}720\text{ cm}^{-1}$ range reflect tetrahedral group (T-site) modes of ferrites, whereas those in the $450\text{--}620\text{ cm}^{-1}$ range represent octahedral group (O-site) modes. The typical appearance of modes is shown as $A_g + E_g + F_{2g}(3)$. The A_g mode corresponds to the symmetric stretching of Fe-O and Ni-O bonds at the tetrahedral group site. The E_g mode corresponds to symmetric bending of Fe-O and Ni-O bonds at the tetrahedral site. The $F_{2g}(2)$ mode is assigned to the asymmetric stretching of Fe-O and Ni-O bonds at the octahedral site. The $F_{2g}(3)$ mode is affected due to the asymmetric bending of Fe-O and Ni-O bonds at the octahedral site and $F_{2g}(1)$ mode is due to the translational motion of the whole tetrahedral group. There is a negligible displacement of metal atoms in modes A_g , E_g and $F_{2g}(3)$ (Graves et al. 1988). According to Fig. 5, the modes of pure nickel ferrite and Co-Mn doped nickel ferrite ($x = 0, 0.02, 0.04$) are given in table with reference of all five active modes $F_{2g}(1)$, E_g , $F_{2g}(2)$, $F_{2g}(3)$ and A_g . From Table 2, it is observed that some of the Raman signals are very broad, suggesting that they may be composed of more than one Raman band and there is shift of Raman peaks towards higher wave number values in $x = 0.02, 0.04$ as compared to those in $x = 0$. The probable explanation of these extra modes is the nickel ferrite lattice. As earlier reported in single crystalline spinel ferrite, observed the particle size increases due to the Raman band shifts to the high frequency and become narrow peak. This behavior is a typical confinement of phonons due to the particle size reduction. Raman spectra for present samples are described in the frequency range of $150\text{--}800\text{ cm}^{-1}$. Figure 5 shows, the Raman spectra of $\text{NiMn}_{0.05}\text{Fe}_{1.5}\text{O}_4$ consist of broadband nearly at $206.97, 328.85, 479.97$ and 570 cm^{-1} and a strong band at 692.27 cm^{-1} . It has been discovered that the Raman band at 692.27 cm^{-1} exhibits a shoulder-like characteristic at a lower wave number (665.88 cm^{-1}) in addition to the previously mentioned single band of Fe_3O_4 (natural ferrite) in the range of $650\text{--}750\text{ cm}^{-1}$. The other low frequency phonon modes are assigned to F_{2g} and E_g modes, which represent the vibration of that site or are caused by metal ions in the octahedral site. These modes correspond to the symmetric and antisymmetric bending of the oxygen atom in the M-O compound at the octahedral sites. The doublet like feature in our samples ascribed to the local cation distribution. Due to the different ionic radii of the Ni and Fe ions, the Fe-O, Ni-O bond distance redistribute between the both sites (tetrahedral and octahedral) resulting in a doublet like structure. The phonon confinement in the materials is effective when the size of the sample is about 20 times larger than the lattice parameter. Raman modes occur and may be considered as a result of the decrease in crystallite size [15].

FTIR Spectroscopy of NCMF Ferrites

FTIR Spectroscopy of the NCMF spinel ferrite has been recorded in the range from 500 cm^{-1} to 4000 cm^{-1} as shown in Fig. 6. NCMF shows the presence of two strong absorption band one attributed by stretching vibration mode of metal-oxygen in tetrahedral sites and other associated with octahedral site which is the common feature of spinel ferrite. The weak band around 418 cm^{-1} is ascribed to the stretching vibration of octahedral metal-oxygen bond and the strong band around 546 cm^{-1} is ascribed to the intrinsic stretching vibration of the tetrahedral metal-oxygen bonds, which are properties of the spinel structure and thus confirm the cubic spinel ferrite formation. For Nickel ferrite pure sample, two main absorption bands of metal-oxygen (Fe-O) stretching vibration observed at 418 and 546 cm^{-1} . The cation distribution of ferrites is predictable by using the following relation (Joshi & Kumar 2016), Interestingly, the characteristic band ν_1 shows a shift to lower and higher frequencies increasing through the substitution Co-contents. It can be seen that the peak position of ν_1 and ν_2 changes by increasing cobalt content and due to Fe vacancy content, but the degree of shift in the ν_1 peak position towards lower frequency is higher than that of the ν_2 peak position This might be also due to the fact that substitution of Co-contents at A site and the Fe ion vacancy mostly occurred at the B sites. The cation distribution of ferrite shows that the Co^{2+} ion occupies the tetrahedral site (A⁻ site) and the Ni^{2+} ion occupies the octahedral site (B⁻ site) while Fe^{3+} ions occupy the octahedral as well

as the tetrahedral site. In the Substitution of Co^{2+} and Mn^{2+} ions in the scheme decreases the amount of Ni^{2+} and increases the amount of Fe^{3+} ions in the octahedral B^- site and shifts the band position (418 cm^{-1}) towards the higher wave number. It is clear from both Fig. 6 (a-b) that there is a shift of absorption band on tetrahedral site towards the higher wavelength or lower wave number. This may be due to the sintering of samples or environmental effect. Furthermore the deficiency in iron and addition of Co are helpful in suppressing the formation of Fe^{2+} ion. The main difference is the position of stretching modes for Fe and Ni (Co), owing to different bond strength of Fe-O and Ni-O, Fe-O bonds are stronger then iron is trivalent and Co-O or Ni-O weaker then these cations is divalent. The bands at $3596\text{--}3746\text{ cm}^{-1}$ can be assigned to O-H stretching vibrations that interact through H bonds that originate in the moisture content of the sample. The bending vibration has been very broad. The reason could be attributed to the distribution of Fe^{3+} ions at tetrahedral sites. The difference in frequencies might be due to change in the bond length between Fe^{3+} and O^{2-} , which are located at octahedral and tetrahedral sites.

UV-Vis spectroscopy of NCMF Ferrites

The optical properties of samples in the optical region (200–800 nm) using UV-Vis spectroscopy. Plot between reflectance and wavelength for all samples are shown in Fig. 7, in which black data line is for pure and red, blue and green line for doped sample. The optical band gap associated with the ferrites is determined through an extrapolation of the linear tendency observed in the spectral dependence of $(\alpha h\nu)^{1/n}$ over a limited range of photon energies $h\nu$ Tauc relation $\alpha h\nu = a(h\nu - E_g)^n$; where α is the absorption coefficient, a is a characteristic parameter of transition which depends on the value of 'n' that can have values 1/2, 2, 3/2, and 3 for allowed direct, allowed indirect, forbidden direct, and forbidden indirect transitions, respectively, E_g denotes the optical band gap energy, h is the Planck constant and ν is visible the incident photons frequency. The direct band gap energy is derived by assuming a direct transition between the edges of the valence band and the conduction band. The meeting point of this straight line on x-axis gives the value of optical band gap. Now the best fit is obtained for $n = 1/2$; the direct and indirect energy gap $x = 0$ shown in Fig. 8 (a-b) and peak at about 1.53eV can be assigned neither to IVCT nor to ISCT transition. The 1.53eV peak is due to the $3T_1(3F) \rightarrow 3A_2(3F)$ CF transition in the Ni^{2+} ions at the tetrahedral sites. The 1.53eV energy band assigned as due to the $3T_2(3F) \rightarrow 3A_2(3F)$ CF transition. In the polar Kerr (Kim et al. 2002) and Faraday (Ostorero et al. 1991) investigations on NiFe_2O_4 similar kinds of evidence were reported for the magneto-optical activity of tetrahedral Ni^{2+} ions near 1eV. Indirect energy band gap Tauc plots is given by Fig. 8(b) Only three significant indirect bands are found in case of Co-Mn doped nickel ferrite at 1.32 eV which corresponds to the $3T_2(3F) \rightarrow 3A_2(3F)$ crystal field transition and IVCT transition between nickel and iron ions of t_{2g} and e_g orbitals respectively i.e. $[\text{Ni}^{2+}] t_{2g} \rightarrow [\text{Fe}^{3+}] e_g$. The Tauc plots for the direct allowed and indirect allowed transition for $x = 0.02$ given in Fig. 8(c-d). The plots are showing the narrow band gap between 1-3eV. The direct energy band 1.15 eV is due to the ISCT i.e. $(\text{Fe}^{3+}) t_{2g} \rightarrow [\text{Fe}^{3+}] t_{2g}$ where () represents the tetrahedral and [] represents the octahedral sites. The energy band 1.15 eV is due to the IVCT between the divalent nickel and trivalent iron ions i.e. $[\text{Ni}^{2+}] t_{2g} \rightarrow [\text{Fe}^{3+}] t_{2g}$. Here both iron and nickel ions are in octahedral site. IVCT transitions, $[\text{Ni}^{2+}] t_{2g} \rightarrow (\text{Fe}^{3+}) e_g$, are expected to appear at about 1.15eV which is beyond the present detection range. The indirect allowed bands found at 0.92eV in Fig. 8(d) for $x = 0.02$. The energy band gap 0.92 eV is because of ISCT between Fe ions i.e. $(\text{Fe}^{3+}) t_{2g} \rightarrow [\text{Fe}^{3+}] t_{2g}$ is due to the IVCT between Ni and Fe ions i.e. $[\text{Ni}^{2+}] t_{2g} \rightarrow [\text{Fe}^{3+}] e_g$. The IVCT transitions, $[\text{Ni}^{2+}] t_{2g} \rightarrow (\text{Fe}^{3+}) e_g$, are expected to appear at about 0.92eV which is beyond the present detection range. The Fig. 8(e-f) is the direct and indirect energy gap Tau plots for NCMF; $x = 0.04$. Peak at about 1.20 eV can be assigned neither to IVCT nor to ISCT transition. The 1.20 eV peak is due to the $3T_1(3F) \rightarrow 3A_2(3F)$ CF transition in the Ni^{2+} ions at the tetrahedral sites. The Indirect energy gap Tauc plots for same sample is given by Fig. 8(f). Only one significant indirect bands are found in case of Co-Mn doped nickel ferrite at 1.17eV which corresponds to the $3T_2(3F) \rightarrow 3A_2(3F)$ crystal field transition and IVCT transition between nickel and iron ions of t_{2g} and e_g orbitals respectively i.e. $[\text{Ni}^{2+}] t_{2g} \rightarrow [\text{Fe}^{3+}] e_g$.

Magnetic hysteresis loops of NCMF Ferrites

Typical magnetic hysteresis loops obtained at RT for cobalt- substituted spinel ferrites $\text{Ni}_{1-x}\text{Co}_x\text{Mn}_{0.05}\text{Fe}_{1.95}\text{O}_4$ for $x = 0, 0.02, 0.04$ shown in Fig. 9, which exhibits a ferromagnetic behavior. The magnetic properties of the spinel ferrites depend on the composition and distribution of cation in the tetrahedral (A^-) and octahedral (B^-) sites. The chemical composition and the particle size play an important role in the determination of the magnetic properties of the samples. In the present work, the Mn^{3+} , Co^{3+} and Ni^{2+} ions predominantly occupied the octahedral sites and saturation magnetization is strongly depends on cation distribution at the (A) and (B) sites. The

variation of saturation magnetization can be explained on the basis of exchange interactions between (A) and (B) sites. The substitution of Fe^{3+} ions can be seen that all the Mn^{3+} , Co^{3+} and Ni^{2+} ions predominantly occupy the octahedral sites of the ferrite sublattice. The coercivity is decrease due to the arrangement of surface effect and its surface anisotropy. As we know with increasing the size of NPs and decreasing the surface area to volume ratio of the nanosized particles, the effect of surface anisotropy decreases. The coercivity of all samples originates from multidomain structure. The multidomain region of the coercivity increases as the particle size decreases. Figure 9(b) indicates that, the saturation magnetization (M_s) coercive force (H_c) of sample $\text{Ni}_{1-x}\text{Co}_x\text{Mn}_{0.05}\text{Fe}_{1.95}\text{O}_4$ for $x = 0, 0.02, 0.04$. As stated before, the H_c is found to increase with the increase in Co doping. This is expected for any ferrimagnetic material due to higher ferromagnetic properties than Mn content. The replacement of Ni^{2+} ions and Co^{3+} ion associated through the A^- site allows the Fe^{3+} ions transfer to the A^- to B^- site and increases the whole magnetic moment. On the other hand, it has been found that the coercive force increases with the doping concentration attributed to the strong magneto-crystalline anisotropy of cobalt ferrite and after doping, the anisotropy of the samples has been increased. Interestingly, on the other hand, M_s shows a non-monotonic behavior as a function of Mo doping. First, M_s Increases from 56.01 to 59.24 emu/g (upon $x = 0.02$ of Co doping) and then decreases at around $x = 0.04$ of Co doping. The same trend in H_c and M_s has been observed at all the temperatures measured and shows that cobalt ferrite sustains its hard magnetic nature (Hossain et al. 2020).

Antifungal activity of NCMF Ferrites.

All treatments inhibited the mycelial growth of the pathogen as compared to control. The results revealed that NCMF for $x = 0.04$ was found to be most effective results in 100% inhibition of the radial growth of *Aspergillus niger* (MT675916) pathogen followed by NCMF for $x = 0.02$ (60%) inhibition; whereas NCMF for $x = 0.00$ showed lowest (20%) inhibition of the radial growth of *Aspergillus niger*. It was observed that the per cent of mycelial inhibition of pathogen was increased with increased in $\text{Ni}_{1-x}\text{Co}_x\text{Mn}_{0.05}\text{Fe}_{1.95}\text{O}_4$ for x concentration of treatments (Fig. 10). The synthesized NCMF for $x = 0, 0.02, 0.04$ nanocomposite can be a potent disinfectant against the pathogenic fungus of *Aspergillus niger* causes maximum post-harvest losses in economically important crops; resulting in decay and rotting in fruits and vegetables. Anti-pathogenic possessions of nanocomposites reveal their biomedical and disinfectant properties. Transition metal-substituted $\text{Co}_{0.5}\text{X}_{0.5}\text{Fe}_2\text{O}_4$ with $X = \text{Cu, Zn, Mn and Ni}$; cobalt ferrite nanoparticles were synthesized using sol gel method and analysed against *E. coli* and *S. aureus* bacterial cultures (Sanpo et al. 2013). Magnetite nanoparticles $\text{NiFe}_2\text{O}_4@Ag$ and $\text{NiFe}_2\text{O}_4@Mo$, were synthesized, and good antifungal activity of $\text{NiFe}_2\text{O}_4@Ag$ nanoparticle were assessed against two plant pathogenic fungi *Alternaria solani* and *Fusarium oxysporum* (Golkhatmi et al. 2017).

Conclusions

In this paper, we report for the first time the successful synthesis of NCMF ferrite using a low-temperature sol gel combustion process with nitrates as cations and citric acid ($\text{C}_6\text{H}_8\text{O}_7$) as the combustion/chelating agent. X-ray diffraction (XRD) patterns of samples single phase cubic spinel structure, similar to that of NiFe_2O_4 . Average crystallite size of pure and Mn-Co doped nickel samples were found to be in the range 36-48.54 nm. Raman analysis demonstrated the shifting of frequency modes with the doping of cobalt, and the intensity of A1-mode decreases which may be due to Ni-O covalent bond. FTIR analysis was revealed two main absorption bands at 418 cm^{-1} and 546 cm^{-1} which correspond to metal oxygen (Fe-O), and stretching vibration of octahedral site and tetrahedral site for 418 cm^{-1} and 546 cm^{-1} bands respectively. The optical direct and indirect band gap of pure nickel ferrite was found in the range of 1.48eV and 1.19eV; showed a redshift of 0.92 eV. The saturation magnetization (M_s) was in the range 52emu/g - 59emu/g, and indication of soft magnetic material. Furthermore, the antifungal efficacy of synthesized NPs was tested against *Aspergillus niger* (MT675916) species. The increased activity is due to varying Cobalt doping, which resulted in an increase in the ratio of surface to volume of NPs, resulting in better microbe interaction. As a result, Cobalt incorporated nickel, manganese ferrite NPs with strong magnetic and antifungal properties have a lot of promise in pharmaceutical and biomedical applications.

Declarations

Conflicts of interest

The authors declare no conflict of interest.

References

Ahmad, N., Sultana, S., Kumar, G., Zuhaib, M., Sabir, S. & Khan, M. Z. (2019). *Journal of Environmental Chemical Engineering* 7: 102804.

Akinremi, C., Omos, N., Adewuyi, S., Idowu, M., Amolegbe, S. & Atayese, A. (2018). *Journal of Chemical Society of Nigeria* 43.

Aly, K. A., Khalil, N., Algamal, Y. & Saleem, Q. M. (2016). *Journal of Alloys and Compounds* 676: 606-612.

Chand, P., Vaish, S. & Kumar, P. (2017). *Physica B: Condensed Matter* 524: 53-63.

Cullity, B. & Stock, S. (2001). Upper Saddle River, NJ: 388.

Deng, M.-M., Zhang, D.-W., Yasmin, A., Liao, J.-Y., He, X.-D. & Chen, C.-H. (2019). *SN Applied Sciences* 1: 72.

Diba, K., Kordbacheh, P., Mirhendi, S., Rezaie, S. & Mahmoudi, M. (2007). *Pakistan journal of medical sciences* 23: 867.

Golkhatmi, F. M., Bahramian, B. & Mamarabadi, M. (2017). *Materials Science and Engineering: C* 78: 1-11.

Graves, P., Johnston, C. & Campaniello, J. (1988). *Materials Research Bulletin* 23: 1651-1660.

Guillemaut, P. & Maréchal-Drouard, L. (1992). *Plant molecular biology reporter* 10: 60-65.

Hossain, A., Sarker, M., Khan, M. & Rahman, M. (2020). *Materials Science and Engineering: B* 253: 114496.

Joshi, S. & Kumar, M. (2016). *Ceramics International* 42: 18154-18165.

Kadam, A., Shinde, S., Yadav, S., Patil, P. & Rajpure, K. (2013). *Journal of Magnetism and Magnetic materials* 329: 59-64.

Khan, S. A., Shahid, S., Ayaz, A., Alkahtani, J., Elshikh, M. S. & Riaz, T. (2021). *International Journal of Nanomedicine* 16: 1757.

Kim, K. J., Lee, H. S., Lee, M. H. & Lee, S. H. (2002). *Journal of Applied Physics* 91: 9974-9977.

Mostaghni, F. & Abed, Y. (2017). *Materials Research* 20: 569-575.

Mukherjee, D., Hordagoda, M., Hyde, R., Bingham, N., Srikanth, H., Witanachchi, S. & Mukherjee, P. (2013). *ACS applied materials & interfaces* 5: 7450-7457.

Naseri, M. G., Saion, E. B., Ahangar, H. A. & Shaari, A. H. (2013). *Materials Research Bulletin* 48: 1439-1446.

Naughton, B. T. & Clarke, D. R. (2007). *Journal of the American Ceramic Society* 90: 3541-3546.

Orozco, C., Melendez, A., Manadhar, S., Singamaneni, S., Reddy, K. M., Gandha, K., Niebedim, I. & Ramana, C. (2017). *The Journal of Physical Chemistry C* 121: 25463-25471.

Ostorero, J., Guillot, M., Leblanc, M. & Rouet, D. (1991). *Journal of Applied Physics* 69: 4571-4573.

Prathapani, S., Jayaraman, T. V., Varaprasadarao, E. K. & Das, D. (2014). *Journal of Applied Physics* 116: 023908.

Pu, S.-Z., Sun, Q., Fan, C.-B., Wang, R.-J. & Liu, G. (2016). *Journal of Materials Chemistry C* 4: 3075-3093.

Rahman, M. T., Vargas, M. & Ramana, C. (2014). *Journal of Alloys and Compounds* 617: 547-562.

Sanpo, N., Berndt, C. C., Wen, C. & Wang, J. (2013). *Acta Biomaterialia* 9: 5830-5837.

Sharma, P., Biswas, P. & Singh, P. (2021). *Journal of Alloys and Compounds*: 159626.

Shobana, M. & Sankar, S. (2009). *Journal of Magnetism and Magnetic materials* 321: 2125-2128.

Velhal, N. B., Patil, N. D., Shelke, A. R., Deshpande, N. G. & Puri, V. R. (2015). *AIP Advances* 5: 097166.

Vincent, J. (1947). *Nature* 159: 850-850.

Zhao, K., Zhou, D., Ping, W. & Ge, J. (2004). *Nat Sci* 2: 52-59.

Tables

Table 1 Values of Lattice Constant, Density, and Particle Size As Determined from XRD for $\text{Ni}_{1-x}\text{Co}_x\text{Mn}_{0.05}\text{Fe}_{1.95}\text{O}_4$ (for $x=0, 0.02, 0.04$)

Co content	Lattice parameter (Å)	X-Ray density (gm/cm ³)	Lattice strain	Crystallite size (nm)
$\text{NiMn}_{0.05}\text{Fe}_{1.95}\text{O}_4$	8.31	5.42	2.51×10^{-3}	48.54
$\text{Ni}_{0.098}\text{Co}_{0.02}\text{Mn}_{0.05}\text{Fe}_{1.95}\text{O}_4$	8.32	5.45	2.32×10^{-3}	48.52
$\text{Ni}_{0.096}\text{Co}_{0.04}\text{Mn}_{0.05}\text{Fe}_{1.95}\text{O}_4$	8.36	5.52	2.31×10^{-3}	44.76

Table 2 Parameters calculated from Raman spectra of $\text{Ni}_{1-x}\text{Co}_x\text{Mn}_{0.05}\text{Fe}_{1.95}\text{O}_4$ ($x = 0, 0.02, 0.04$) by using intense peaks.

Modes (↓)	Sample (→)	$\text{NiMn}_{0.05}\text{Fe}_{1.95}\text{O}_4$	$\text{Ni}_{0.098}\text{Co}_{0.02}\text{Mn}_{0.05}\text{Fe}_{1.95}\text{O}_4$	$\text{Ni}_{0.096}\text{Co}_{0.04}\text{Mn}_{0.05}\text{Fe}_{1.95}\text{O}_4$
		Raman Shift (cm ⁻¹) ±		
F2g(1) (translationl motion)	Tetrahedral Group Site	206	208	208
Eg (symmetric bending)	Tetrahedral Group Site	329	331	331
F2g(2) (asymmetric stretching)	Octahedral Group Site	480	483	485
F2g(3) (asymmetric bending)	Octahedral Group Site	570	572	575
Ag (symmetric stretching)	Tetrahedral Group Site	693	696	698

Table 3 Energy band gap for direct and indirect allowed transitions for ($\text{Ni}_{1-x}\text{Co}_x\text{Mn}_{0.05}\text{Fe}_{1.95}\text{O}_4$ for $x = 0, 0.02, 0.04$)

Transitions	$\text{NiMn}_{0.05}\text{Fe}_{1.95}\text{O}_4$	$\text{Ni}_{0.098}\text{Co}_{0.02}\text{Mn}_{0.05}\text{Fe}_{1.95}\text{O}_4$	$\text{Ni}_{0.096}\text{Co}_{0.04}\text{Mn}_{0.05}\text{Fe}_{1.95}\text{O}_4$
Direct	1.48eV	1.53 eV	1.15 eV
Indirect	1.19 eV	1.32 eV	0.92 eV

Figures

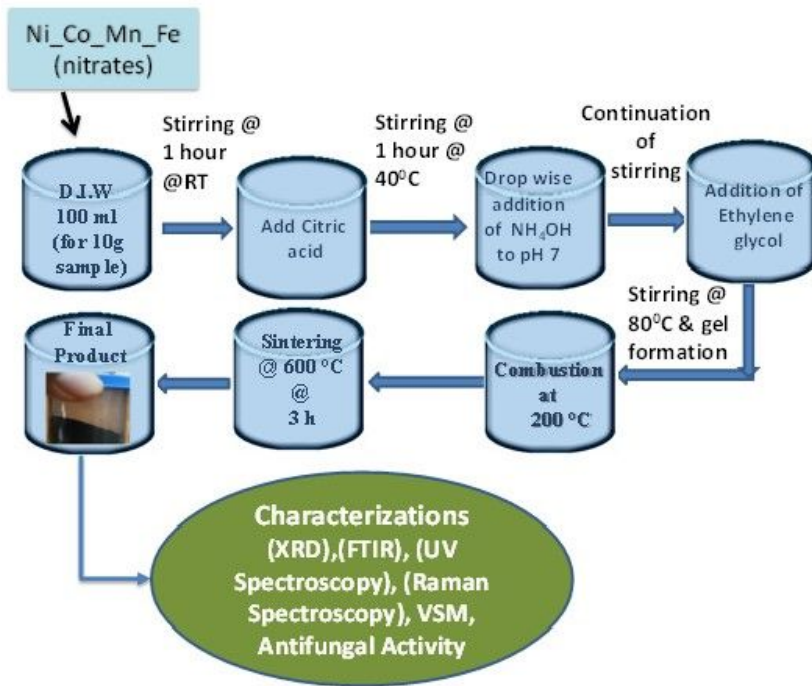


Figure 1

Systematic synthesis process of $Ni_{1-x}Co_xMn_{0.05}Fe_{1.95}O_4$ ($x = 0, 0.02, 0.04$ samples using a low-temperature sol gel combustion process.

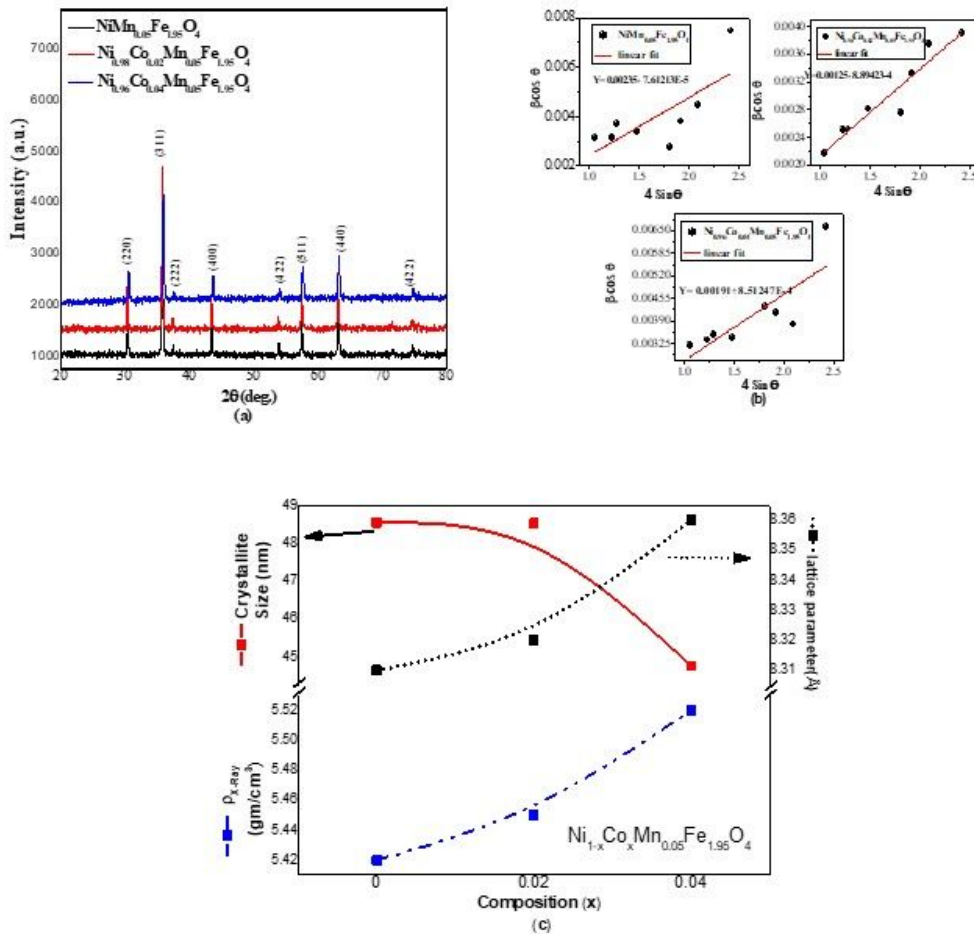


Figure 2

(a) XRD patterns of the Ni_{1-x}CoxMn_{0.05}Fe_{1.95}O₄ (where x = 0, 0.02, 0.04) (NCMF) ferrites as a function of x. The peaks identified and their assignment are as indicated. (b) Williamson-Hall plot to find the lattice strain (ϵ) of samples; (c) lattice parameter - (Right Y-axis - variation of lattice parameter with Co content (x) and Cobalt incorporation induced lattice expansion compared to that of pure NMF (x=0) is evident.); density (left Y-axis- the linear increase in density is due to the incorporation of heavier Co substituting for Fe in the ferrite); crystallite size (upper left Y-axis- The variation of average crystallite size. The crystallite size increase with increasing Co content in NCMF is evident) as function of Co concentration (x).

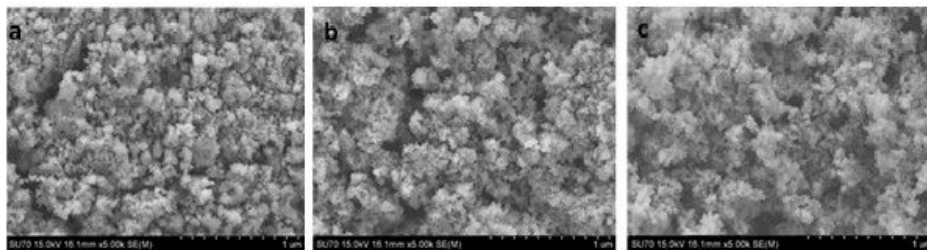


Figure 3

SEM picture for Ni_{1-x}CoxMn_{0.05}Fe_{1.95}O₄ NPs (a) at x=0 (b) x=0.02 and (b) x=0.04 respectively

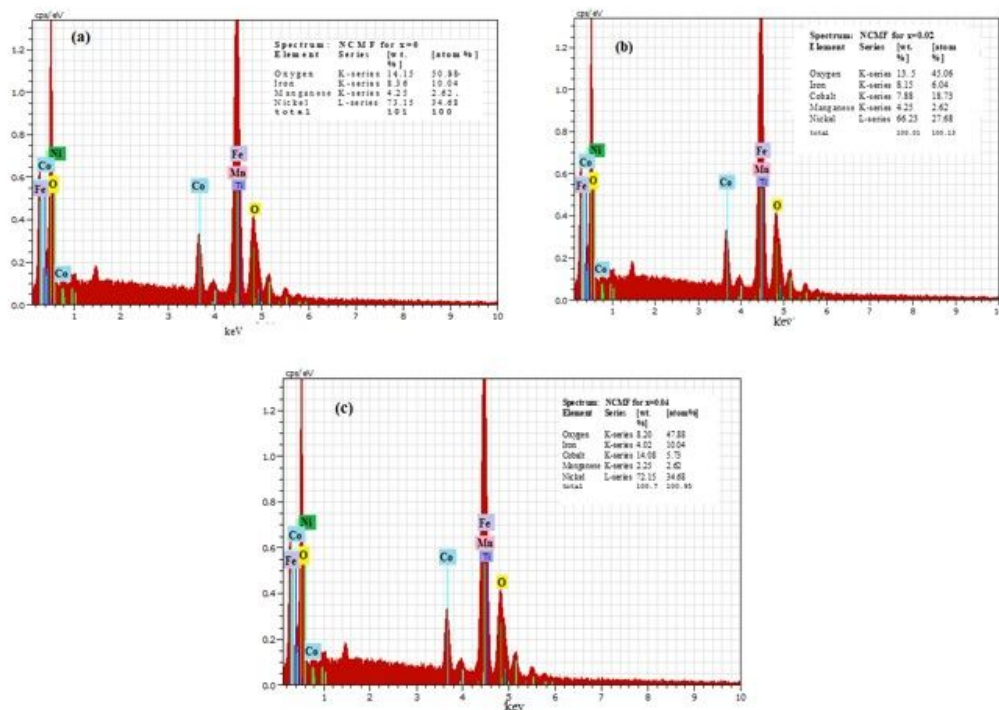


Figure 4

Energy Dispersive X-ray (EDX) for Ni_{1-x}CoxMn_{0.05}Fe_{1.95}O₄ NPs (a) at x=0 (b) x=0.02 and (b) x=0.04 respectively

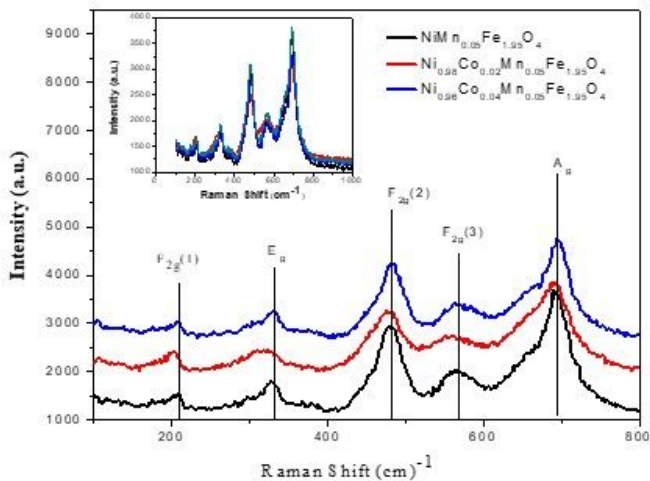


Figure 5

Raman spectra for $\text{Ni}_{1-x}\text{Co}_x\text{Mn}_{0.05}\text{Fe}_{1.95}\text{O}_4$ ($x=0, 0.02, 0.04$)

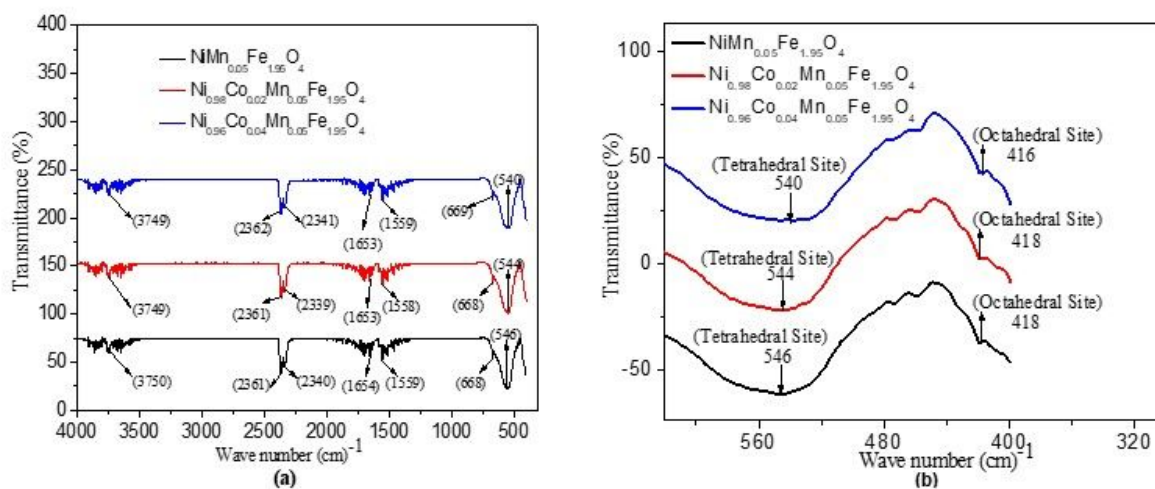


Figure 6

(a-b)-FTIR Spectra for $\text{Ni}_{1-x}\text{Co}_x\text{Mn}_{0.05}\text{Fe}_{1.95}\text{O}_4$ ($x=0.02, 0.04$) recorded in the range from 400 cm^{-1} to 4000 cm^{-1} and (b) - shows the presence of two strong absorption band one attributed by stretching vibration mode of metal-oxygen in tetrahedral sites and other associated with octahedral site which is the common feature of spinel ferrite.

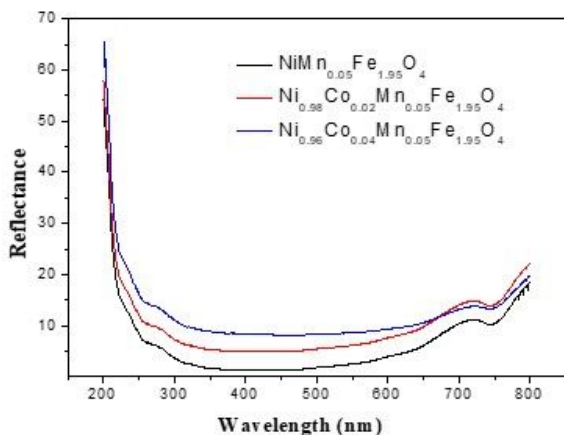


Figure 7

The optical properties in the optical region (200-800 nm) using UV-Vis Absorption spectroscopy; Plot between reflectance and wavelength for Ni_{1-x}Co_xMn_{0.05}Fe_{1.95}O₄ (x = 0.02, 0.04).

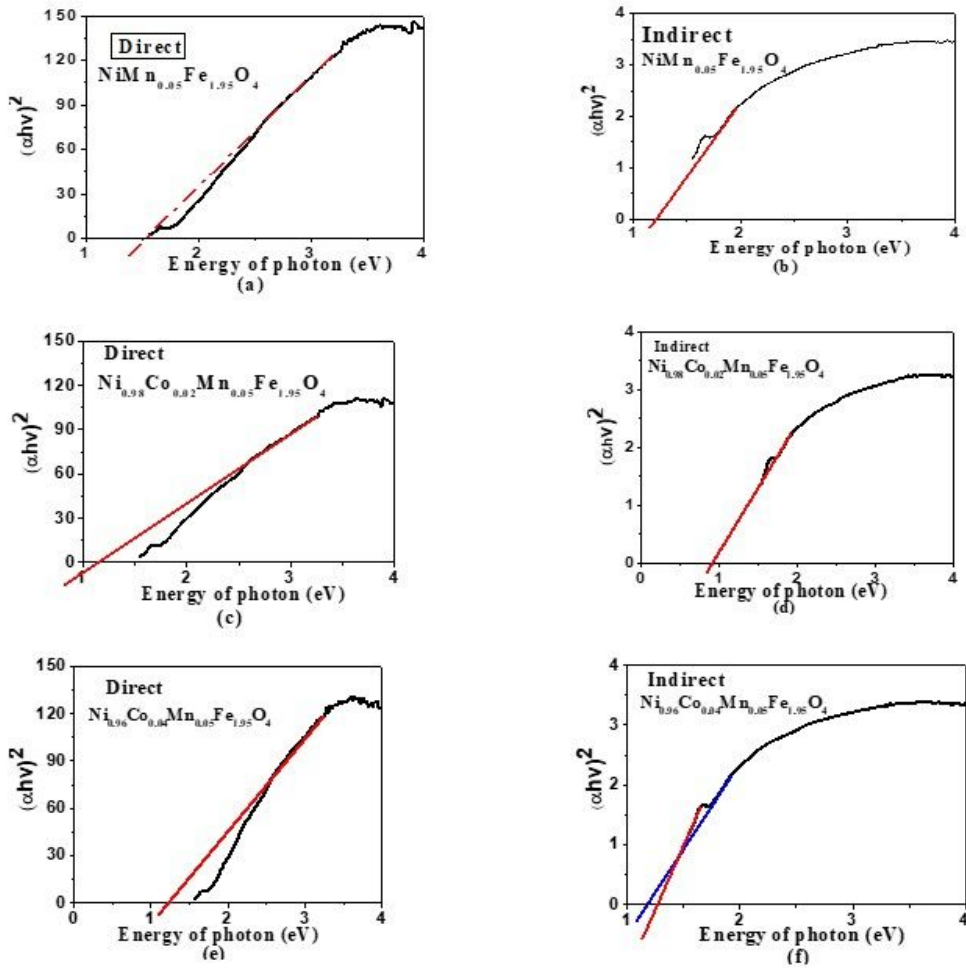


Figure 8

(a-f) Plot of $(\alpha h\nu)^2$ as a function of photon energy (eV) for Ni_{1-x}Co_xMn_{0.05}Fe_{1.95}O₄ (x = 0.02, 0.04)

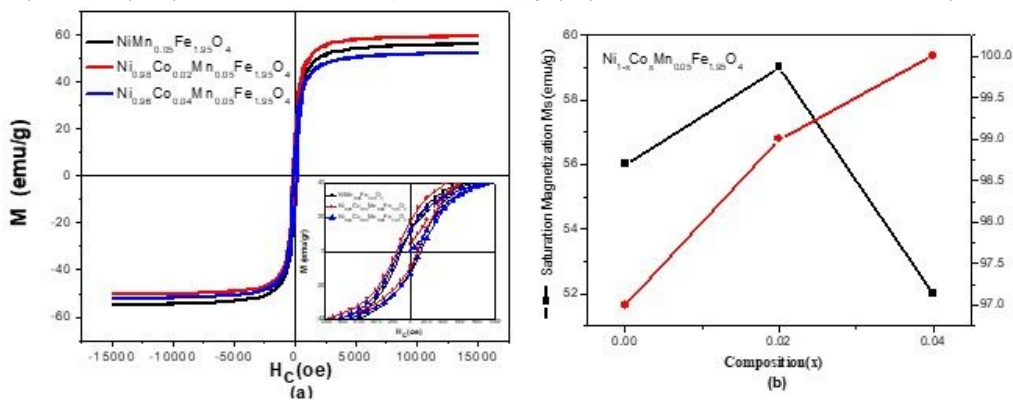


Figure 9

(a) Typical magnetic hysteresis loops obtained at RT for cobalt- substituted spinel ferrites Ni_{1-x}Co_xMn_{0.05}Fe_{1.95}O₄ for x = 0, 0.02, 0.04 (b)-The variation of coercive field H_c (right Y-axis) and saturation magnetization M_s (left Y-axis, measured from M-H curves) as a function of Co doping (0- 0.04).

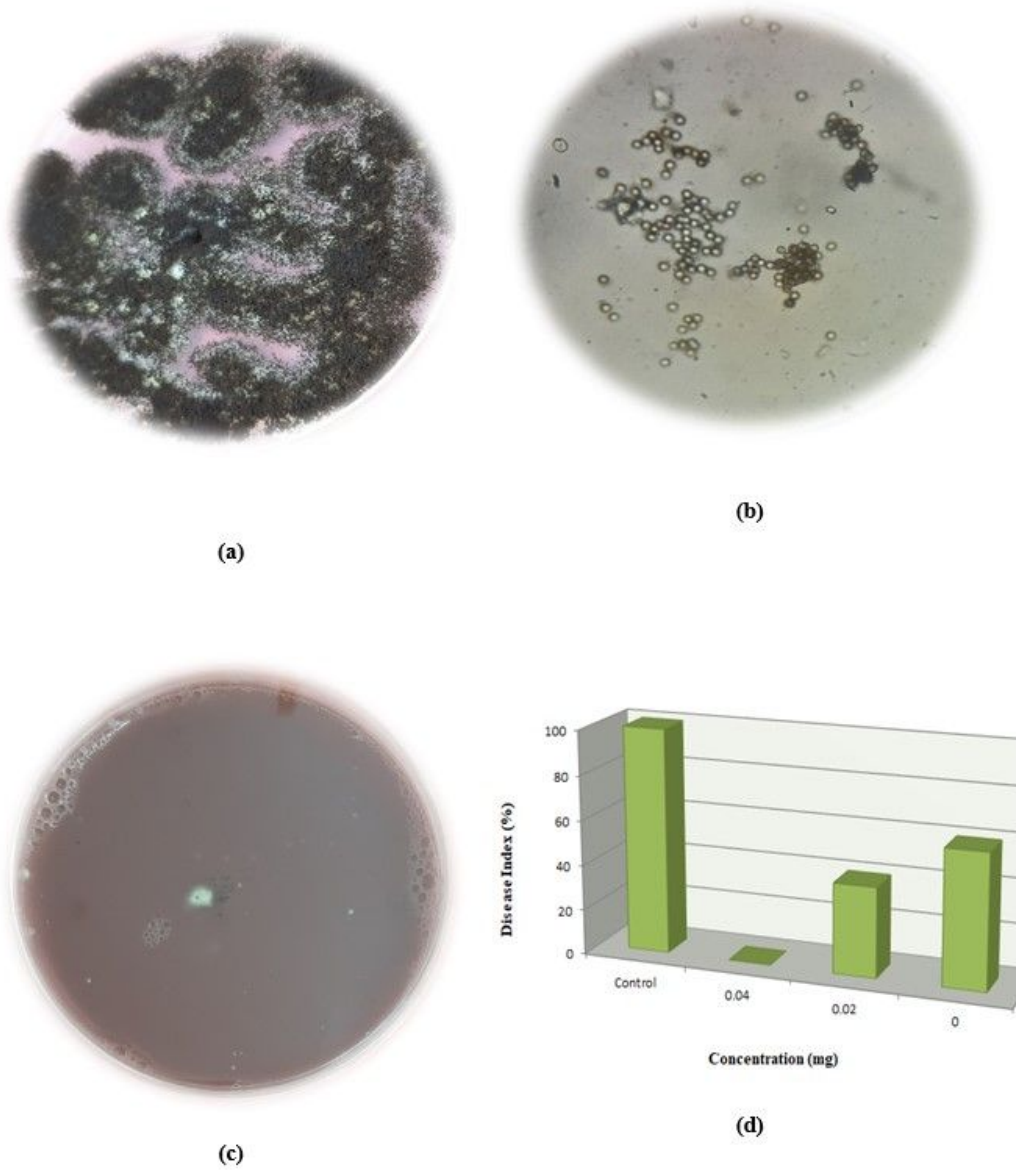


Figure 10

(a) Control of *Aspergillus niger* after 7 days; (b) Microscopic structure of *Aspergillus niger*; (c) 100 % inhibition of *Aspergillus niger* by NiMn_{0.05}Fe_{1.95}O₄ X=0.04 Concentration after 7 days (d) Disease reduction (%) in radial growth of *Aspergillus niger*